








Article

Effects of Substrate Temperature on Optical, Structural, and Surface Properties of Metal–Organic Vapor Phase Epitaxy-Grown MgZnO Films

Jiamin Liu ^{1,†} , Deng Xie ^{2,†}, Zhe Chuan Feng ^{1,3,4,*} , Manika Tun Nafisa ³ , Lingyu Wan ⁵ , Zhi-Ren Qiu ⁶, Dong-Sing Wu ⁷ , Chuanwei Zhang ¹, Jeffrey Yiin ³, Hao-Hsiung Lin ⁸, Weijie Lu ⁹, Benjamin Klein ³ , Ian T. Ferguson ³ and Shiyuan Liu ^{1,10,*} 

- ¹ State Key Laboratory of Intelligent Manufacturing Equipment and Technology, Huazhong University of Science and Technology, Wuhan 430074, China; jiaminliu@hust.edu.cn (J.L.); chuanweizhang@hust.edu.cn (C.Z.)
 - ² School of Electronic & Electrical Engineering and Physics, Fujian University of Technology, Fuzhou 350000, China; dengx@fjut.edu.cn
 - ³ Southern Polytechnic College of Engineering and Engineering Technology, Kennesaw University, Marietta, GA 30060, USA; mnafisa@students.kennesaw.edu (M.T.N.); jyiin@kennesaw.edu (J.Y.); bklein8@kennesaw.edu (B.K.); ianf@kennesaw.edu (I.T.F.)
 - ⁴ Science Exploring Laboratory, Arbour Glenn Drive, Lawrenceville, GA 30043, USA
 - ⁵ Center on Nano-Energy Research, Guangxi Key Laboratory for the Relativistic Astrophysics, Institute of Science and Technology for Carbon Peak & Neutrality, School of Physical Science & Technology, Guangxi University, Nanning 530004, China; lyw2017@gxu.edu.cn
 - ⁶ State Key Laboratory of Optoelectronic Materials and Technologies, School of Physics, Sun Yat-sen University, Guangzhou 510275, China; stsqzr@mail.sysu.edu.cn
 - ⁷ Department of Applied Materials and Optoelectronic Engineering, National Chi Nan University, Puli, Nantou 54561, Taiwan; dsw@ncnu.edu.tw
 - ⁸ Department of Electrical Engineering, Graduate Institute of Photonics and Optoelectronics, National Taiwan University, Taipei 10617, Taiwan; hlin@ntu.edu.tw
 - ⁹ Hexagonal Scientific Laboratory, LLC, Dayton, OH 45459, USA; wlu@hsl-mat.com
 - ¹⁰ Optics Valley Laboratory, Wuhan 430074, China
- * Correspondence: zfceng6@kennesaw.edu (Z.C.F.); shyliu@hust.edu.cn (S.L.); Tel.: +86-18377178295 (Z.C.F.); +86-027-87559543 (S.L.)
- † These authors contributed equally to this work.



Citation: Liu, J.; Xie, D.; Feng, Z.C.; Nafisa, M.T.; Wan, L.; Qiu, Z.-R.; Wu, D.-S.; Zhang, C.; Yiin, J.; Lin, H.-H.; et al. Effects of Substrate Temperature on Optical, Structural, and Surface Properties of Metal–Organic Vapor Phase Epitaxy-Grown MgZnO Films. *Nanomaterials* **2024**, *14*, 1957. <https://doi.org/10.3390/nano14231957>

Academic Editor: Alexander Kromka

Received: 5 November 2024
Revised: 29 November 2024
Accepted: 3 December 2024
Published: 5 December 2024



Copyright: © 2024 by the authors. Licensee MDPI, Basel, Switzerland. This article is an open access article distributed under the terms and conditions of the Creative Commons Attribution (CC BY) license (<https://creativecommons.org/licenses/by/4.0/>).

Abstract: MgZnO possesses a tunable bandgap and can be prepared at relatively low temperatures, making it suitable for developing optoelectronic devices. $Mg_xZn_{1-x}O$ ($x \sim 0.1$) films were grown on sapphire by metal–organic vapor phase epitaxy under different substrate-growth temperatures T_s of 350–650 °C and studied by multiple characterization technologies like X-ray diffraction (XRD), spectroscopic ellipsometry (SE), Raman scattering, extended X-ray absorption fine structure (EXAFS), and first-principle calculations. The effects of T_s on the optical, structural, and surface properties of the $Mg_{0.1}Zn_{0.9}O$ films were studied penetratively. An XRD peak of nearly 35° was produced from $Mg_{0.1}Zn_{0.9}O$ (0002) diffraction, while a weak peak of ~36.5° indicated MgO phase separation. SE measurements and analysis determined the energy bandgaps in the 3.29–3.91 eV range, obeying a monotonically decreasing law with increasing T_s . The theoretical bandgap of 3.347 eV, consistent with the SE-reported value, demonstrated the reliability of the SE measurement. Temperature-dependent UV-excitation Raman scattering revealed 1LO phonon splitting and temperature dependency. Zn–O and Zn–Zn atomic bonding lengths were deduced from EXAFS. It was revealed that the surface Mg amount increased with the increase in T_s . These comprehensive studies provide valuable references for $Mg_{0.1}Zn_{0.9}O$ and other advanced materials.

Keywords: $Mg_{0.1}Zn_{0.9}O$; metal–organic vapor phase epitaxy; X–ray diffraction; spectroscopic ellipsometry; Raman spectroscopy; enharmonic phonon process; synchrotron radiation; near-edge X–ray absorption fine structure; X–ray photoelectron spectroscopy

1. Introduction

In recent decades, benefiting from the advantages of easily tunable bandgaps larger than 3.2 eV, visible-spectral transparency, considerable exciton-binding energy, good conductivity, non-toxicity, etc., the research and development of ZnO-based materials and structures have attracted significant attention and achieved fruitful results [1–14]. MgZnO ternary alloys, as typical ZnO-based materials, are direct wide-bandgap semiconductors with broad applications in electronic and optoelectronic fields [9,13,15,16]. Ternary $\text{Mg}_x\text{Zn}_{1-x}\text{O}$ (MZO) alloys with tunable Mg compositions have recently been developed for various high-voltage transparent thin-film transistors and other types of devices [2,9,16]. Meanwhile, by reducing the defect density, the thermal and bias stabilities of MZO alloys can be improved significantly [9,16], which enables much broader applications in novel optoelectronic devices [17]. In these hot and frontier topics involving MZO, tunable bandgap energy between 3.3 and 7.8 eV is realized by changing the Mg or Zn composition in the host ZnO or MgO materials; the corresponding bandgap-based applications have been of the most fundamental concern [16–28]. For instance, MZO alloys are promising in deep ultraviolet (UV) photodetectors [3], UV light-emitting diodes (LEDs) and transparent thin-film transistors [6], UV thin-film phototransistors [21], n-MZO/p-GaN heterojunction diodes for UV EL applications [24], and bulk acoustic wave (BAW) resonators [25]. Wurtzite structural MZO with $x < 0.25$ is an optimal candidate for applications in optoelectronic devices, such as UV phototransistors, photodetectors, and detectors for UV environmental monitoring [18]. Kumar, P. et al. [2] reported that $\text{Mg}_{0.1}\text{Zn}_{0.9}\text{O}$ films have room-temperature (RT) ferromagnetism, which is helpful for spintronic applications for energy conversion and storage applications. Also, MZO alloys can be used to construct MZO/CdSe/CdTe solar cells with high performance [5] and fabricate MZO/CdSe/CdTe solar cells with improved device characteristics [8]. Usually, MZO films can be prepared via different technologies, such as metal-organic vapor phase epitaxy (MOVPE) [27], molecular-beam epitaxy (MBE) [15,26], electrodeposition [4], atomic layer deposition (ALD) [23], sol-gel and spin-coating methods [24], magnetron sputtering [22], and so on. Substrates used for epitaxy include sapphire [9,22], Si [12,22], and glass [4–6,21]. However, how fabrication processes such as substrate-growth temperature affect the surface, structure, and optoelectronic properties of $\text{Mg}_x\text{Zn}_{1-x}\text{O}$ remains to be investigated.

Several studies have focused on the comprehensive performance characterization and modulation mechanism discovery of $\text{Mg}_x\text{Zn}_{1-x}\text{O}$ alloys. In these investigations, the variation in the lattice constants of wurtzite $\text{Mg}_x\text{Zn}_{1-x}\text{O}$ alloys with Mg compositions was characterized using the X-ray diffraction method [6,21,28]. D. C. Tsai et al. [6] used XRD to capture the film crystallinity of crystallite size variations and studied the integral intensity, FWHM, and grain size of MgZnO films as a function of the Al_2O_3 content in targets [6]. C. Y. Tsay et al. [21] obtained very narrow grazing incidence XRD peak widths for sol-gel-deposited undoped and Ga-doped $\text{Mg}_{0.2}\text{Zn}_{0.8}\text{O}$ thin films. Extended X-ray absorption fine structure (EXAFS) spectroscopy, considered a powerful technique, was used to probe the crystalline structures and electronic bonding states of $\text{Mg}_x\text{Zn}_{1-x}\text{O}$ materials [29,30]. L. Bergman et al. [31] employed ultraviolet photoluminescence and Raman scattering to study $\text{Mg}_x\text{Zn}_{1-x}\text{O}$ nano-powders with $0 \leq x \leq 0.26$. L. Wang et al. [32] used high-resolution transmission electron microscopy and X-ray diffraction spectroscopy to characterize the growth state of cubic $\text{Mg}_{0.21}\text{Zn}_{0.79}\text{O}/\text{MgO}$ multiple quantum wells. In these studies, the physical properties of $\text{Mg}_x\text{Zn}_{1-x}\text{O}$ materials were explored under specific substrate temperature conditions, such as 450 °C or 300 °C [27], which motivated us to further investigate the effects of different substrate temperatures.

In the present work, we performed a comprehensive investigation of the optical, structural, and surface properties of a series of $\text{Mg}_{0.1}\text{Zn}_{0.9}\text{O}$ films on a sapphire substrate prepared by metal-organic vapor phase epitaxy (MOVPE), with different substrate-growth temperatures T_s of 350, 450, 550, and 650 °C, respectively. These were studied by multiple characterization techniques like high-resolution X-ray diffraction (HR-XRD), spectroscopic ellipsometry (SE), UV (325 nm)-excitation Raman spectroscopy (RS), synchrotron radiation

(SR), extended-edge X-ray absorption fine structure (EXAFS) spectroscopy, X-ray photoelectron spectroscopy (XPS), and first-principle calculations. The effects of substrate-growth temperature on the optical, structural, and surface properties of $\text{Mg}_{0.1}\text{Zn}_{0.9}\text{O}$ films were investigated thoroughly. Detailed studies of Urbach's tailing energy E_U [7,21,22] were performed via the SE method.

2. Materials and Methods

2.1. Preparation and Characterization of $\text{Mg}_{0.1}\text{Zn}_{0.9}\text{O}$ Films

Experimental $\text{Mg}_{0.1}\text{Zn}_{0.9}\text{O}$ epitaxial materials were prepared by MOVPE (EMCORE D-180 system, Veeco, New York, NY, USA), with sources of DEZn [$\text{Zn}(\text{C}_2\text{H}_5)_2$ purity 99.9999%], CpMg [$(\text{C}_5\text{H}_5)_2\text{Mg}$ purity 99.99%], and oxygen gas [O_2 (99.999% purity)] plus Ar carry-gas (99.9999% purity). The substrate was set as c-sapphire due to its advantages of low cost, high quality, and suitability for mass production. In order to prepare the high-quality $\text{Mg}_{0.1}\text{Zn}_{0.9}\text{O}$, the inner, middle, and outer gas flow rates, as shown in reference [27], were precisely controlled, accompanied by organometallic sources and O_2 being introduced into the reactor separately and mixing before entering the chamber. The total flows were kept at 2800 sccm, with a pressure of 20 Torr in the reactor, as described in [27]. The Mg amount in $\text{Mg}_{0.1}\text{Zn}_{0.9}\text{O}$ could be adapted using the control of the CpMg flow rate. In the current work, the sapphire-substrate temperatures T_s were set as 350 °C, 450 °C, 550 °C, and 650 °C, respectively, enabling a slight modulation of the crystalline quality and the surface Mg amount.

Using XRD observations, the Mg concentration, i.e., $x(\text{Mg})$ in the MZO, was determined as about 0.10 for these four MZO films, which were named MZO350, MZO450, MZO550, and MZO650, respectively. Then, the structural, surface, and optical properties of these $\text{Mg}_{0.1}\text{Zn}_{0.9}\text{O}$ films were evaluated by high-resolution X-ray diffraction (HR-XRD), Raman scattering, and spectroscopic ellipsometry (SE), respectively. Correspondingly, HR-XRD spectra (MRD 5-crystal system, Phillips, USA) were captured and analyzed to reveal the crystallite size, lattice strain, and dislocation density of these samples.

The ellipsometric spectra captured using a Mueller-matrix ellipsometer (ME-L, Wuhan Eoptics Technology Co., Ltd., Wuhan, China) were analyzed to obtain the optical constants, bandgap, thickness, and surface roughness. Ellipsometric parameter spectra ($\psi(\lambda)$ and $\Delta(\lambda)$) covering a spectrum of 193–1690 nm were captured using the multi-incidence angle probing mode, in which three incidence angles of 65°, 70°, and 75° were used to ensure the convergence of the inverse problem solution involved. A stratified optical model, consisting of an air ambient layer, a roughness layer, an isotropic layer, and the sapphire substrate layer, was used to fit the measured $\psi(\lambda)$ and $\Delta(\lambda)$ spectra of the four samples. Following the bottom-up principle, the dielectric functions of the sapphire substrate were first modeled using the Cauchy oscillators, and the dielectric functions of the $\text{Mg}_x\text{Zn}_{1-x}\text{O}$ layer were represented by parametrized Tauc–Lorentz oscillators. A two-phase effective-medium approximation model was used to describe the dielectric functions of the surface roughness layer on the $\text{Mg}_x\text{Zn}_{1-x}\text{O}$ layer, and the dielectric functions of the air ambient layer were set to 1. By analyzing the ellipsometric spectra, via the forward optical model built in J. A. Woollam's CompleteEASE software M2000, the complex refractive index and the thickness could be determined for four $\text{Mg}_x\text{Zn}_{1-x}\text{O}$ films. The thicknesses of these $\text{Mg}_{0.1}\text{Zn}_{0.9}\text{O}$ were determined as 87 nm, 82 nm, 74 nm, and 77 nm, accompanying low mean square errors in the fitting of ellipsometric spectra. Variable-temperature Raman scattering spectra were captured using a micro-Raman system (inVia™, Renishaw, UK) combined with a variable-temperature loading module (THMS600, LinKam, Salford, UK). The Raman scattering spectra were obtained under ultraviolet excitation from a He-Cd laser at a wavelength of 325 nm. Further theoretical analyses, based upon the 3- and 4-phonon processes, on the variable-temperature Raman spectra were performed, revealing 1-LO phonon splitting and temperature dependency.

Extended X-ray absorption fine structure (EXAFS) spectroscopy was employed to acquire the atomic bonding lengths of $\text{Mg}_{0.1}\text{Zn}_{0.9}\text{O}$ films, revealing the crystalline structure

and electronic bonding states. The angle-dependent Zn K-edge EXAFS spectra were captured using the fluorescence-mode 17C beamline under the incidence angle range of 15° – 90° at the synchrotron radiation research center in Hsinchu. In addition, X-ray photoelectron spectroscopy (XPS) was performed by a ULVAC-PHI PHI 5000, with the excitation source as Al K α (1486.7 eV) radiation and with the photo-electron take-off angle as 45° . All the spectra were calibrated to a C1s peak at 284.6 eV.

2.2. First-Principle Calculations

Although multi-scale computational studies combined with density functional theory have partially explained the growth mechanism and structural selectivity of many typical wide-bandgap semiconductors [33–35], research on the accurate calculation of the bandgap of $\text{Mg}_x\text{Zn}_{1-x}\text{O}$ and the influence of possible defect states still needs to be improved. All the first-principle calculations based on density functional theory were carried out with the Vienna Ab initio simulation package (VASP v5.4.4), to obtain the band structure, bandgap, and density of state. The exchange-correlation potential was described using the Perdew–Burke–Ernzerhof (PBE) functional of generalized gradient approximation (GGA) based on the projected augmented wave (PAW) pseudopotentials. The original ZnO with a hexagonal wurtzite structure was built by setting the space-group symmetry of $P_{63}mc$ and lattice parameters of $a = b = 3.249 \text{ \AA}$ and $c = 5.205 \text{ \AA}$. After the geometry optimization of the lattice cell, the ZnO supercell $2 \times 5 \times 1$ was modeled in a configuration containing 40 atoms (20 Zn atoms and 20 O atoms). A doping Mg atom (10 at. % concentration) was chosen, as shown in Figure 1a. Then, we used the PBE functional based on the PAW pseudopotential with an energy cutoff of 600 eV and a $5 \times 5 \times 3$ Γ -centered k-point mesh, ensuring the reliable optimization of the geometric structure and the approximative calculation of the physical properties. Meanwhile, the GGA + U scheme with appropriate on-site Coulomb interaction U can correct the Zn-3d electronic orbits, which enables the accurate calculation of the bandgap. The reference U perturbation for the Zn-3d orbitals is set to $U_{\text{Zn}3d} = 12.6 \text{ eV}$. Also, the effects of Mg doping in the ZnO crystallite structure on the electronic and optical properties were evaluated and analyzed. When calculating the projected density of states, a denser $10 \times 10 \times 6$ Γ -centered k-point mesh was used. The convergence criteria of force and total energy were 0.01 eV/\AA and 10^{-6} eV , respectively.

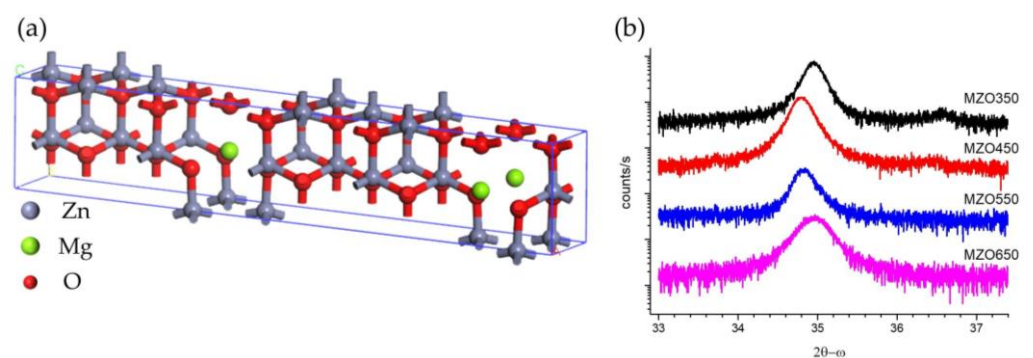


Figure 1. Crystalline structure of $\text{Mg}_{0.1}\text{Zn}_{0.9}\text{O}$: (a) Lattice structure of $\text{Mg}_{0.1}\text{Zn}_{0.9}\text{O}$; (b) HR-XRD spectra (0002) of four $\text{Mg}_{0.1}\text{Zn}_{0.9}\text{O}$.

3. Results

3.1. High-Resolution X-Ray Diffraction Measurement and Calculation

Figure 1b presents the HR-XRD (0002) scanning results for four MgZnO/sapphire samples, indicating that all MgZnO samples grown on the sapphire substrates show an apparent polarity (0002) orientation. The peak near 35° is from MgZnO (0002) diffraction [15,16], while a weak peak near 36.5° appears for two samples with lower (350°C and 450°C) growth temperatures. The cubic ZnO possesses a maximum solid solubility of 35% for hexagonal MgO [31], which is related to the XRD peak near 36.5° . This indicates that MgO phase separation could occur at lower substrate-growth temperatures, due to the

incorporation of MgO causing zincblende (111) face diffraction. However, the XRD peaks near 36.5° are much weaker than the XRD peaks near 35° , indicating a shallow magnitude of MgO phase separation in MZO350 and MZO450. It can also be seen that the wurtzite (0002) peak for MZO350 and MZO650 is located at 35.0° of 2θ , while those for MZO450 and MZO550 are at 34.7° of 2θ . This indicates that the c-axis lattice constants of MZO350 and MZO650 are slightly larger than those of MZO450 and MZO550, which reflects that too-low and too-high substrate-growth temperatures could lead to a larger c-axis lattice constant of the MgZnO film.

The crystal phase and lattice constant of these samples can be evaluated from their XRD data. From the Bragg formula $2d\sin\theta = n\lambda$, $2\theta = 35.0^\circ$ indicates a lattice constant of 5.127 \AA , consistent with the literature value 5.206 \AA [36]. The XRD peak near 36.5° corresponds to a lattice constant of 4.261 \AA , representative of hexagonal MgO in cubic ZnO [31] and indicative of MgO phase separation having occurred at a lower substrate-growth temperature. To analyze the structural properties of four MgZnO samples and compare their crystal qualities, the HR-XRD (0002) peak and FWHM values from Figure 1b were obtained by Gaussian fitting, and those are listed in Table 1. Detailed quantitative calculations were performed to obtain the crystallite size D , lattice strain ϵ , and dislocation density δ of $\text{Mg}_{0.1}\text{Zn}_{0.9}\text{O}$ [4–6], as shown in Table 1.

Table 1. XRD (0002) 2θ peak and FWHM; calculated values of crystallite size, lattice strain, and dislocation density; SE-deduced film thickness, bandgap E_g , and Urbach energy E_U of four MgZnO (MZO) films.

Sample No.	MZO350	MZO450	MZO550	MZO650
Substrate-growth temperature (T_s)	350 °C	450 °C	550 °C	650 °C
Peak 2θ (0002) (°)	35.00	34.80	34.82	34.96
FWHM 2θ (0002) (°)	0.526	0.710	0.513	0.763
Crystallite size D (nm)	15.84	11.73	16.24	10.92
Lattice strain ϵ ($\times 10^{-3}$)	2.19	2.96	2.14	3.18
Dislocation density $\delta = 1/D^2$ ($\times 10^{-3} \text{ nm}^{-2}$)	3.99	7.27	3.79	8.39
Thickness (nm) from SE	87	82	74	77
E_g (eV) from SE	3.91	3.69	3.48	3.29
E_U (meV) from SE	466	93	116	211

The FWHMs for four MgZnO films are located in the range of 0.51° – 0.76° , compatible with MgZnO film XRD FWHM values of 0.5° – 1.0° from D. C. Tsai et al. [6], implying good crystal quality. Four MgZnO samples have a low threading dislocation density between 3.8 and $8.4 \times 10^{-3} \text{ nm}^{-2}$. The sample MZO550, grown at the substrate-growth temperature of 550°C , possesses the largest crystallite size and the lowest lattice strain and dislocation density. This phenomenon might be attributed to the modulating effects of substrate-growth temperature on the MgZnO crystalline state, which is similar to the observations of the annealing temperature effects reported by C.L. Heng et al. [24]. They found that the XRD (0002) peak's FWHM decreases from 0.391° to 0.157° with the annealing temperature increasing from 600°C to 900°C , corresponding to the average size of MgZnO nanocrystals increasing from 21.0 nm to 52.4 nm . It can be seen that their XRD values [21,24] are superior to ours listed in Table 1, which indicates that we still need to further improve the growth of our MgZnO film materials.

3.2. Spectroscopic Ellipsometry Measurement and Analysis for $\text{Mg}_{0.1}\text{Zn}_{0.9}\text{O}$ Films

Spectroscopic ellipsometry (SE) measures the relationships of polarization states (psi Ψ and delta Δ) for the incidence and reflection of light versus the wavelength from a sample. The roughness, thickness, refractive index n , and extinction coefficient k of $\text{Mg}_{0.1}\text{Zn}_{0.9}\text{O}$ films were derived from SE data. SE spectra of $\text{Mg}_{0.1}\text{Zn}_{0.9}\text{O}$ samples are fitted by using J. A. Woollam Co. CompleteEASE software. In the model, the surface roughness is modeled by a Bruggeman effective medium approximation. The optical constants of

sapphire are taken from [37] and kept fixed during the fittings. By adjusting all parameters in the $\text{Mg}_{0.1}\text{Zn}_{0.9}\text{O}$ layer, the best-fitted SE data for four samples were achieved. The film thickness and surface roughness for all $\text{Mg}_{0.1}\text{Zn}_{0.9}\text{O}$ samples with minimum errors can be obtained. A comparative measurement of SE and cross-section scanning-electron microscopy (SEM) on the thicknesses of AlN thin layers were performed [38], which confirmed the accuracy of the SE technological determination of the nanometer-scale film thicknesses. Therefore, the thicknesses of our $\text{Mg}_{0.1}\text{Zn}_{0.9}\text{O}$ films determined by SE and listed in Table 1 are feasible and reliable.

Figure 2a–d present the fitting results of Ψ and Δ , and Figure 2a1–d1 show the optical constants n and k of the four $\text{Mg}_{0.1}\text{Zn}_{0.9}\text{O}$ samples. The calculated Ψ and Δ curves are matched well with the corresponding experimental spectra for all three incidence angles of 60° , 65° , and 70° . The fitted film thicknesses of the four samples are listed in Table 1. In the meanwhile, we can obtain the absorption coefficient $\alpha(\lambda) = 4\pi k / \lambda$ from the curve of the extinction coefficient k versus the wavelength λ . Then, by drawing the curves of $(\alpha h\nu)^2$ versus the photon energy $h\nu$ and carrying out a linear interpolation for these four curves [21], the bandgap values could be determined from the intersection points between the interpolation line and the x-axis. The interpolation results are presented in Figure 3, accompanying the bandgaps E_g of 3.91 eV, 3.69 eV, 3.48 eV, and 3.29 eV (with error bars of about +0.02 eV). The corresponding results are also listed in Table 1. Through the linear fitting of the bandgap E_g versus the substrate-growth temperature T_s , the temperature dependency of the bandgap can be determined via the following empirical formula,

$$E_g = -0.002T_s + 4.628, \quad (1)$$

where the coefficient of determination R^2 and the residual sum of squares RSS are 0.9989 and 2.3×10^{-4} , implying a satisfactory fitting analysis in Figure 3c. The fitting results show that the substrate-growth temperature has a linear modulation effect on the bandgap of $\text{Mg}_{0.1}\text{Zn}_{0.9}\text{O}$, manifested as a monotonically decreasing law. Meanwhile, the energy band structure and the electronic density of state are calculated using first-principle simulations, as shown in Figure 3d. It can be easily found that the valence band maxima and conduction band minimum are located at the gamma point, which implies a direct bandgap of 3.347 eV. The theoretical bandgap is consistent with the measurement value reported by the ellipsometry analysis, indicating the reliability of spectroscopic ellipsometry-based characterizations.

It can be observed from Figure 3 that an exponential absorption band tail exists below the band edge in these four $\text{Mg}_{0.1}\text{Zn}_{0.9}\text{O}$ samples, which may result from the structural disorder accompanying electron–phonon coupling [38,39]. This band tail, named the Urbach energy E_U , can be determined by the following analysis of the curves of the absorption coefficient α versus the photon energy $h\nu$ [38–40],

$$E_U^{-1} = d[\ln \alpha(h\nu)]/d(h\nu), \quad (2)$$

Therefore, the Urbach energy E_U can be acquired from the reciprocal of the slope on the linear part for the curves of the logarithm $\ln(\alpha)$ versus the photon energy $h\nu$ [40]. Figure 4 exhibits four $\text{Mg}_{0.1}\text{Zn}_{0.9}\text{O}$ samples grown at 350–650 °C, showing the relationships of absorption coefficients and their logarithm versus photon energy, i.e., $\alpha \sim h\nu$ and $\ln[\alpha(h\nu)] \sim h\nu$ spectra, which finally lead to the determination of E_U . The obtained E_U are listed into Table 1. The lowest- T_s sample (MZO350) has a large E_U of 466 meV, and the highest- T_s sample (MZO650) has the 2nd-largest E_U of 211 meV, while the other two samples, with T_s of 450 °C and 550 °C, possess E_U values of 93 meV and 117 meV, respectively. These results are consistent with those from D.-C. Tsai et al. [6] and C.-Y. Tsay et al. [21].

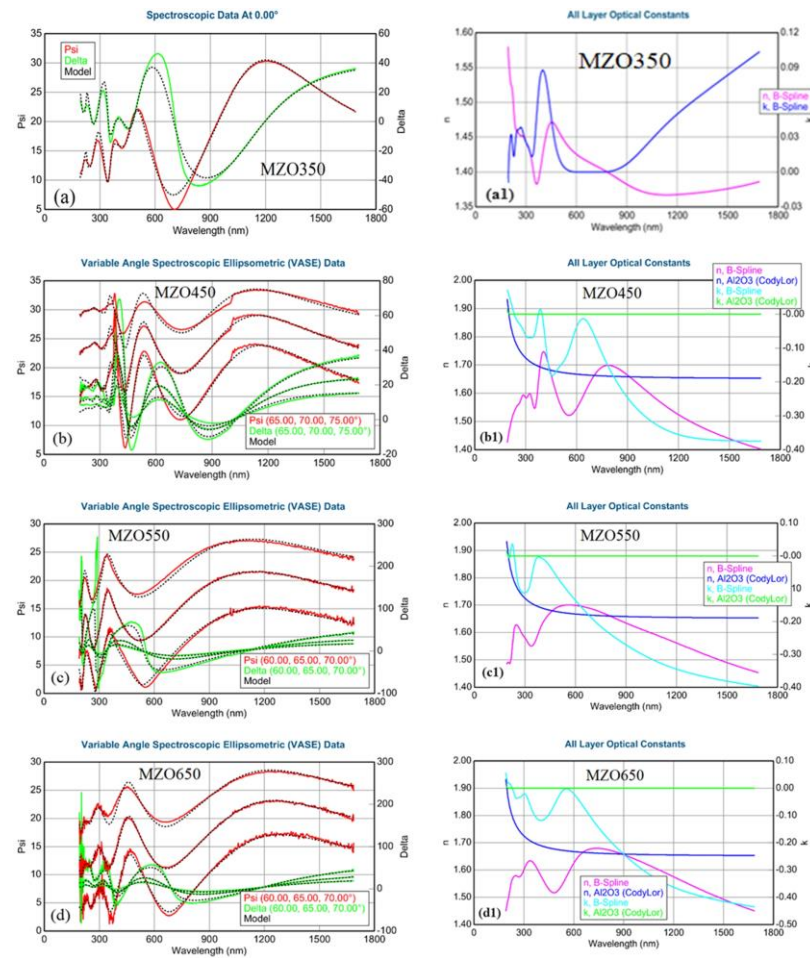


Figure 2. SE psi and delta experimental and fitting n and k spectra of four MgZnO/sapphire samples. (a–d) Fitting results of psi and delta for MZO350 (a), MZO450 (b), MZO550 (c), and MZO650 (d). (a1–d1) Complex refractive indexes for MZO350 (a1), MZO450 (b1), MZO550 (c1), and MZO650 (d1).

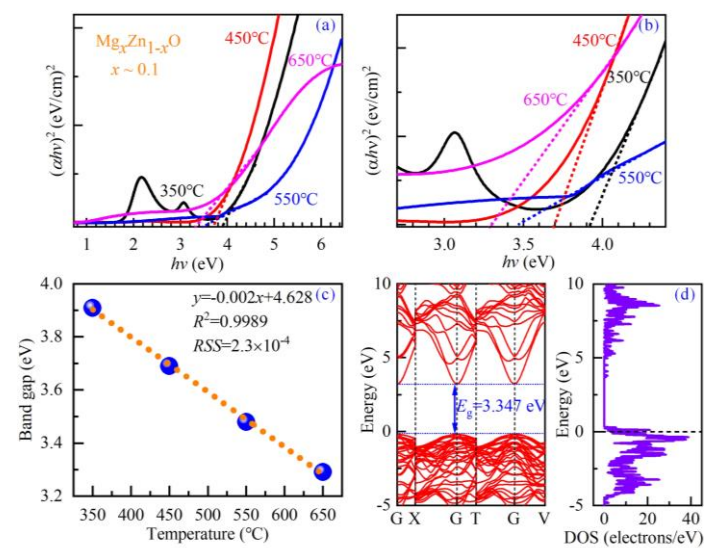


Figure 3. SE-deduced $(ahv)^2 \sim hv$ spectra of four MgZnO/sapphire samples of MZO350, MZO450, MZO550, and MZO650: (a) in the wide energy range of 0.7–6.5 eV, and (b) in 2.7–4.4 eV, showing their bandgap E_g clearly. (c) The substrate-growth temperature dependency of the bandgap energy, and (d) the theoretical band structure determined via the first-principle calculations.

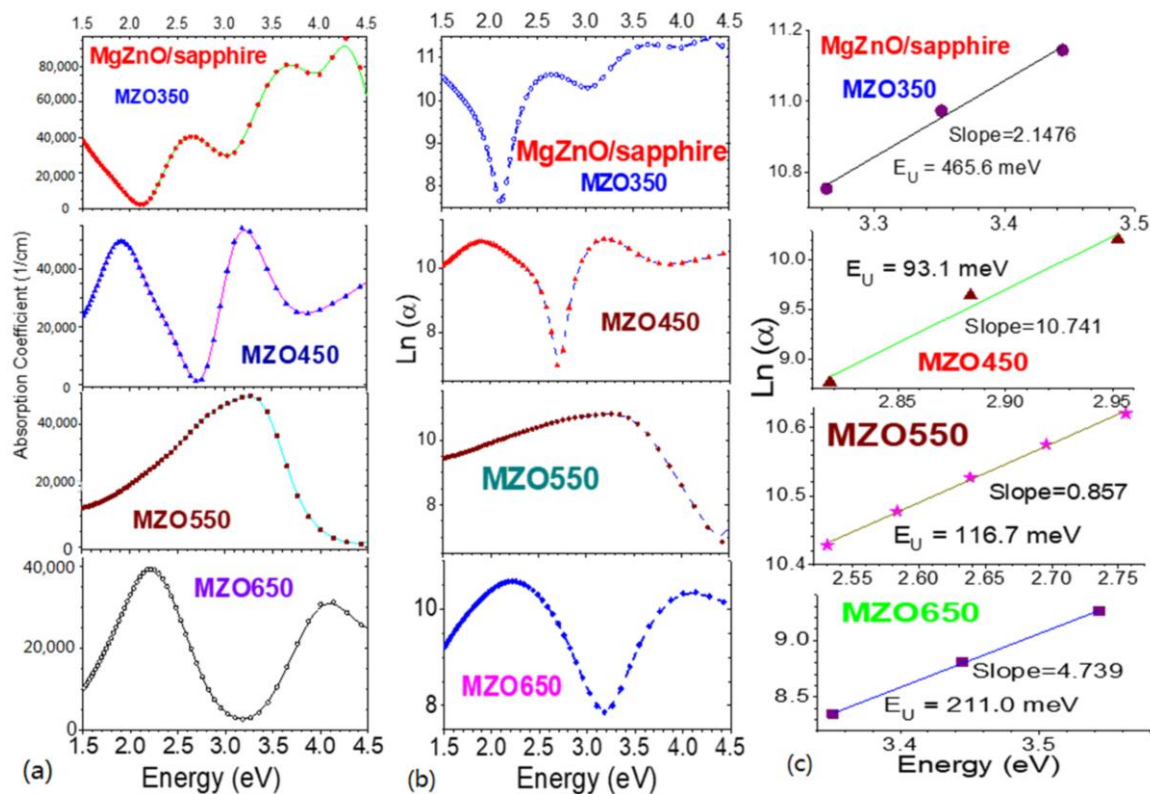


Figure 4. Relationships of absorption coefficient α with photon energy $h\nu$ (a) and $\ln[\alpha(h\nu)]$ with photon energy $h\nu$ (b), and E_U determination (c), for four MgZnO samples of MZO350-MZO650, respectively. Symbols indicate experimental and calculation data. Connecting lines in the left and middle columns are guides for the eyes.

When correlating the Urbach tail energy E_U and the XRD (0002) peak's FWHM in these four $\text{Mg}_{0.1}\text{Zn}_{0.9}\text{O}$ samples, it can be easily noted that MZO550 possesses the narrowest XRD (0002) peak's FWHM, lowest dislocation density, and near-lowest E_U . A close correlation exists between the SE-derived E_U and the XRD FWHM/dislocation density, which implies that the properties in the area near the band edge are related to crystal quality.

3.3. UV (325 nm) Excitation Raman Scattering and Temperature Behavior

Figure 5 shows 325 nm wavelength laser-excited Raman spectra of four $\text{Mg}_{0.1}\text{Zn}_{0.9}\text{O}$ samples. Because of the $\text{Mg}_{0.1}\text{Zn}_{0.9}\text{O}$ samples' thickness of less than 100 nm, the Raman scattering spectra in the visible band showed robust features from the sapphire substrate [15], overwhelming the $\text{Mg}_{0.1}\text{Zn}_{0.9}\text{O}$ signals. Meanwhile, the 325 nm wavelength laser-excited Raman measurements overcame these difficulties. The excitation photon energy of 3.815 eV matched the samples' bandgaps in 3.4–3.9 eV, showing that a resonant enhancement of the Raman longitudinal optical (LO) mode intensities was achieved [31].

Figure 5a presents the 1-LO and 2-LO spectra under the 325 nm wavelength laser excitation. In comparison with the pure ZnO 1-LO at 577 cm^{-1} and 2-LO at 1154 cm^{-1} [31], our $\text{Mg}_{0.1}\text{Zn}_{0.9}\text{O}$ samples' 1-LOs shifted to high frequencies of 14–28–30 cm^{-1} and 2-LOs shifted by 19–54–64 cm^{-1} , respectively. With the T_s increase of 350–450–550 $^{\circ}\text{C}$, the 1-LO and 2-LO frequencies shifted monotonically, and accompanying this, the shift amounts increased. Two dim peaks appeared at 415.5 and 748.7 cm^{-1} in the sample MZO550, caused by the sapphire substrate, which was not found in the other two samples. These appeared because the MZO550 sample had a film thickness of 74 nm, lower than 87 nm for MZO350 and 82 nm for MZO450, from Table 1.

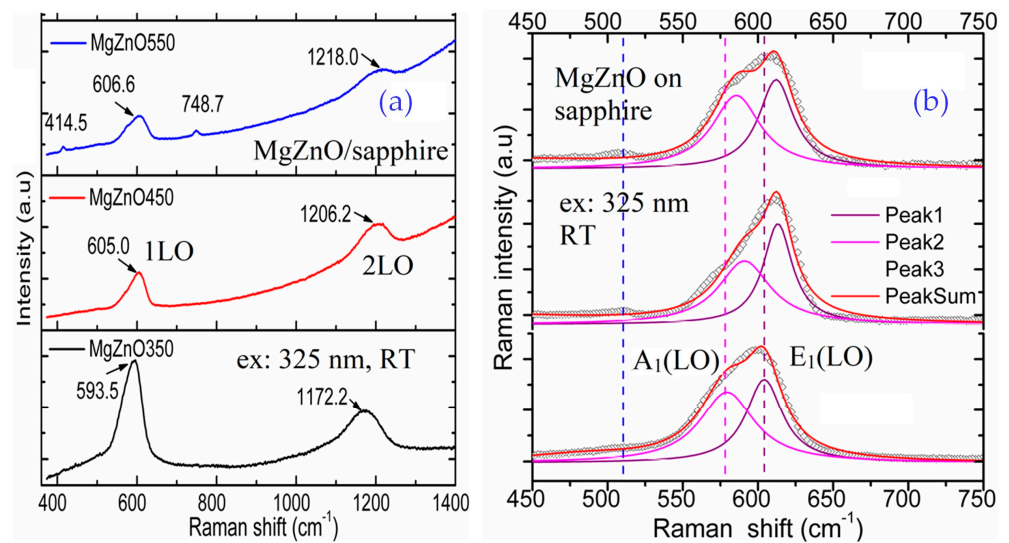


Figure 5. UV 325 nm laser-excited Raman spectra at room temperature of three $\text{Mg}_{0.1}\text{Zn}_{0.9}\text{O}$ samples for (a) 1–LO and 2–LO modes, and (b) Gaussian fits on 1–LO with $A_1(\text{LO})$ and $E_1(\text{LO})$.

It can be observed that all the 1-LO modes in Figure 5a have obvious asymmetric line shapes, which can be recognized as a mixed A_1 - E_1 symmetry phonon or a quasi-LO mode [31]. The mixing and broadening are indicative of both inhomogeneous alloy broadening and the presence of defects [31]. Each 1-LO mode can be deconvoluted into two Gaussian peaks, i.e., $A_1(\text{LO})$ and $E_1(\text{LO})$ modes, which are shown in Figure 5b. J. Huso et al. previously carried this out for $\text{Mg}_{0.2}\text{Zn}_{0.8}\text{O}$ nanoalloys [41], where the nanoalloys' Raman spectrum was well-fitted to the two peaks at 574 cm^{-1} and 601 cm^{-1} , with a separation of 27 cm^{-1} .

Besides $A_1(\text{LO})$ and $E_1(\text{LO})$ modes, there is a weak mode near 510 cm^{-1} , indicated by a dashed blue straight line in Figure 5a. Similar weak features near the Raman shift positions were observed by C. Bundesmann et al. [42], when they studied Raman scattering spectroscopy of $\text{Mg}_x\text{Zn}_{1-x}\text{O}$ films and attributed it to the Mg in ZnO. Accordingly, we also tentatively assign the weak mode at $\sim 510\text{ cm}^{-1}$ to Mg in ZnO.

It can be observed from Figure 5b that from MZO350-MZO450-MZO550, the $A_1(\text{LO})$ peak frequency varies in V-shape, while the $E_1(\text{LO})$ peak frequency shows a monotonic blue shift. The split between the $A_1(\text{LO})$ and $E_1(\text{LO})$ peaks, $\Delta\omega = \omega[A_1(\text{LO})] - \omega[E_1(\text{LO})]$, varies with the variation in the substrate-growth temperature. The physical mechanisms underlying the splitting and the $A_1(\text{LO})/E_1(\text{LO})$ shifts are still under investigation. K. V. S. Ganesha et al. [43] predicted that the Raman line frequency shift in the LO phonon mode would be related to the oxygen defects, interstitial zinc, and free carriers. Meanwhile, J. Huso et al. [41] pointed out that phonon dynamics due to the order–disorder state of the alloy is a very plausible mechanism. They further demonstrated that possible mechanisms of LO line broadening relevant to the MgZnO alloy include granular morphologies in $\text{Mg}_x\text{Zn}_{1-x}\text{O}$ films that may introduce structural defects such as grain boundaries and dangling bonds [44], compositional fluctuation that results in inhomogeneous broadening, and crystal anharmonicity. It is indicated that E_1 is the main symmetry component in the quasi-LO mode [31]. Therefore, it can be reasonably inferred that the $E_1(\text{LO})$ mode is influenced by varying T_s less than the $A_1(\text{LO})$ mode, which leads to the $E_1(\text{LO})$ mode frequency alternating less with T_s than that of the $A_1(\text{LO})$ mode, as shown in Figure 5b.

To further explore the thermodynamic characteristics, we performed variable-temperature Raman measurements and analyses on these three $\text{Mg}_{0.1}\text{Zn}_{0.9}\text{O}$ samples. Figure 6 exhibits temperature-dependent Raman spectra of the MZO350 sample, measured in 80–530 K. The same experiments were also performed for the other two MgZnO samples, MZO450 and MZO550. The Raman peak near 600 cm^{-1} can be deconvoluted into $A_1(\text{LO})$ and $E_1(\text{LO})$ modes, similar to that shown in Figure 5b. In Figure 6, two dashed lines indicate

the variations in these two modes. It can be seen that the split between $A_1(\text{LO})$ and $E_1(\text{LO})$, $\Delta\omega = \omega[A_1(\text{LO})] - \omega[E_1(\text{LO})]$, is decreased with the temperature increasing from 80 K to 530 K.

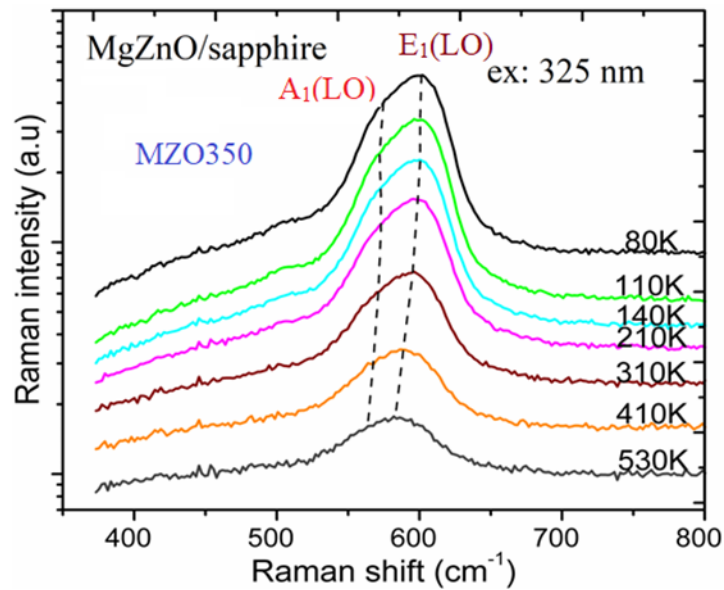


Figure 6. Temperature-dependent Raman spectra of the MZO350 sample between 80 and 530 K.

C. Bundesmann et al. [42] indicated that for lattice vibrations with A_1 and E_1 symmetries, the atoms move parallel and perpendicular to the c -axis, respectively. This means that the $A_1(\text{LO})$ mode describes the phonon vibration along the c -axis, while the $E_1(\text{LO})$ mode describes that perpendicular to the c -axis. Our experimental data in Figure 6 reveal that with T increasing from 80 K to 530 K, the lattice constant along the c -axis varies less than that perpendicular to the c -axis, i.e., the lattice constant c of $\text{Mg}_{0.1}\text{Zn}_{0.9}\text{O}$ varies less with T than the lattice constants of a and b . Further theoretical exploration was carried out on this anharmonic process. A model involving three- and four-phonon processes was used to fit the temperature-dependent Raman shift and width. The temperature-dependent Raman frequency $\omega(T)$ can be modeled as the following formula [45–47],

$$\omega(T) = \omega_0 + \omega^{(1)}(T) + \omega^{(2)}(T), \quad (3)$$

where ω_0 is the phonon frequency at temperature $T = 0$ K, $\omega^{(1)}(T)$ is the contribution from linear thermal expansion, and $\omega^{(2)}(T)$ represents the contribution due to phonon coupling. The second term $\omega^{(1)}(T)$ can be denoted as,

$$\omega^{(1)}(T) = \omega_0 \cdot \left\{ \exp \left[-\gamma \int_0^T [\alpha_c(t) + 2\alpha_a(t)] dt \right] - 1 \right\}, \quad (4)$$

where γ is the Gruneisen parameter for the phonon mode, which presents the anharmonicity of the crystal lattice, and $\alpha_c(t)$ and $\alpha_a(t)$ are the linear thermal expansion coefficients along the c - and a -axes, respectively. The third term $\omega^{(2)}(T)$ can be expressed as,

$$\omega^{(2)}(T) = M_1 \cdot \left\{ 1 + \sum_{i=1}^2 \frac{1}{\exp(x_i) - 1} \right\} + M_2 \left\{ 1 + \sum_{j=1}^3 \left[\frac{1}{\exp(y_j) - 1} + \frac{1}{[\exp(y_j) - 1]^2} \right] \right\}, \quad (5)$$

where M_1 and M_2 are empirical parameters for fits. The x_i and y_j values satisfy $\sum x_i = \sum y_j = \hbar\omega_0$. The first term of $\omega^{(2)}(T)$ denotes the three-phonon process, and the second describes the four-phonon process. During the data-fitting procedure, we took fixed values

of $x = x_1 = x_2 = \hbar\omega_0/2$ and $y = y_1 = y_2 = \hbar\omega_0/3$. The temperature dependence of the Raman frequency $\omega(T)$ can be simplified as,

$$\omega(T) = \omega_0 + \omega^{(1)}(T) + \omega^{(2)}(T) = \omega_0 \cdot \exp\left[-3\gamma\int_0^T \alpha(t)dt\right] + M_1 \cdot \left[1 + \frac{2}{e^x - 1}\right] + M_2 \cdot \left[1 + \frac{3}{e^y - 1} + \frac{3}{(e^y - 1)^2}\right], \quad (6)$$

where ω_0 , M_1 , and M_2 are the parameters for fits. Figure 7 shows the fitting results for the curves of the Raman shift versus T of three $\text{Mg}_{0.1}\text{Zn}_{0.9}\text{O}$ samples, accompanying the fitting parameters listed in Table 2. The results indicate that the $E_1(\text{LO})$ fitting below 300 K is good but with noticeable error bars at high temperatures, of 400–530 K. Meanwhile, for $A_1(\text{LO})$, only MZO450 has good fitting results below 300 K, but with noticeable error bars in other cases.

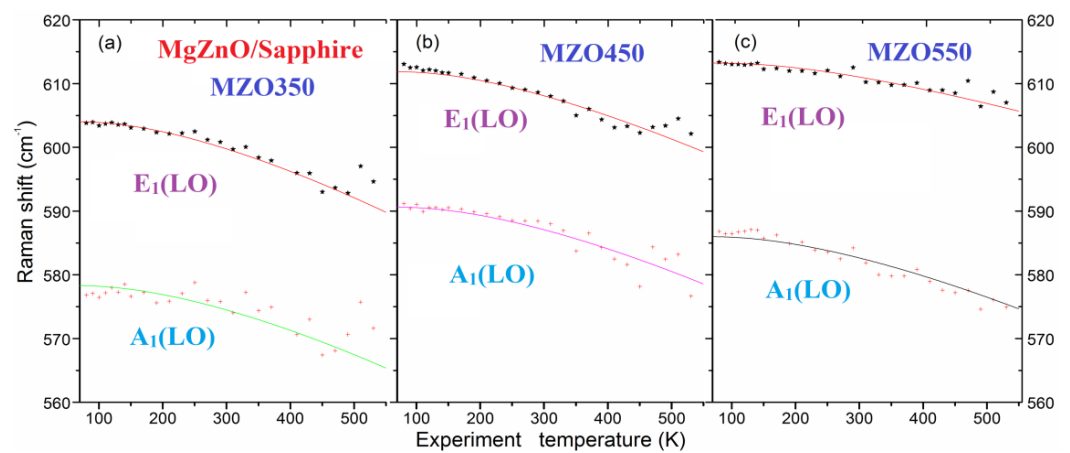


Figure 7. Fitting results of the Raman shift versus T of the $E_1(\text{LO})$ and $A_1(\text{LO})$ for three $\text{Mg}_{0.1}\text{Zn}_{0.9}\text{O}$ samples of MZO350 (a), MZO450 (b), and MZO550 (c), respectively. Symbols are for experimental data, and fitted results from Equation (6) are represented by solid lines.

Table 2. VT Raman peak fitting parameters.

Parameters		MZO350	MZO450	MZO550
$A_1(\text{LO})$	ω_0	580.2	592.4	587.6
	M_1	−1.48	−1.42	−1.33
	M_2	−0.52	−0.47	−0.41
	M_1/M_2	2.85	3.02	3.24
$E_1(\text{LO})$	ω_0	606.8	614.4	614.1
	M_1	−2.35	−2.24	−0.89
	M_2	−0.55	−0.42	−0.14
	M_1/M_2	4.27	5.33	6.36

The line width Γ , i.e., FWHM, of Raman modes can be deduced from anharmonic interactions. Similar to the interpretation of the temperature-dependent Raman frequency $\omega(T)$, the temperature dependency of the Raman line width $\Gamma(T)$ can be given by [45–47],

$$\Gamma(T) = \Gamma_0 + N_1 \cdot \left[1 + \frac{2}{e^x - 1}\right] + N_2 \cdot \left\{1 + \frac{3}{e^y - 1} + \frac{3}{(e^y - 1)^2}\right\}, \quad (7)$$

where Γ_0 is the mode line width at 0 K due to impurity and defect scattering. Quantities N_1 and N_2 are fitting parameters. The second and third terms of $\Gamma(T)$ represent three- and four-phonon processes, respectively. Equations (3)–(7) have been successfully used

in analyzing the temperature-dependent Raman behaviors of GaN [45], ZnO [46], and 4H-SiC [47].

Figure 8 presents fitting results obtained by applying Equation (7) to the temperature-dependent width $\Gamma(T)$ in 60–530 K for the three samples (MZO350, MZO450, and MZO550), accompanying the fitting parameters listed in Table 3. This shows that the error bars in Figure 8 are large, and only rough trends with T are obtained. The trend of rough matching between the measurement and fitting data implies that the temperature dependency of the Raman shift could mainly be due to lattice expansion from the thermal dynamics process and the anharmonic process from three- and four-phonon coupling.

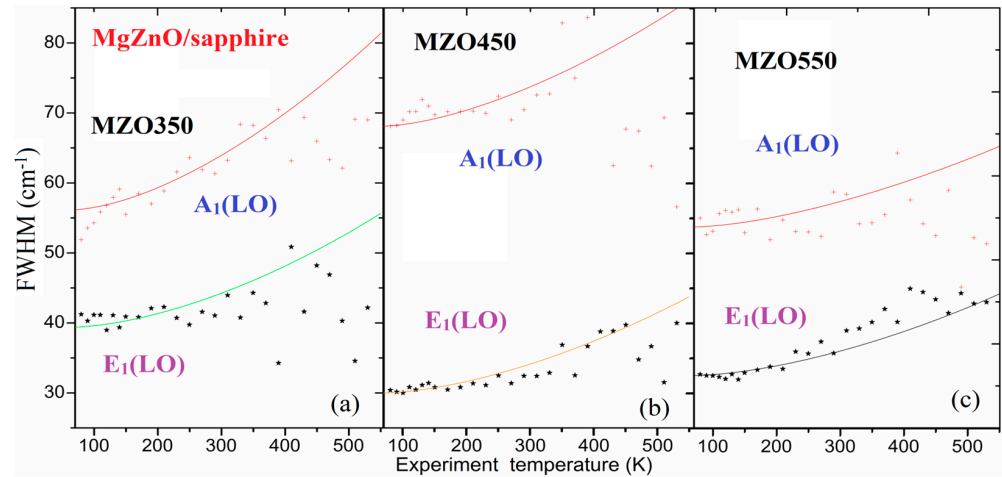


Figure 8. Fitting results of the Raman shift versus T of $A_1(\text{LO})$ and $E_1(\text{LO})$ for three MZO350 (a), MZO450 (b), and MZO550 samples (c), respectively. Symbols correspond to the experimental Raman data, and solid lines represent the fitted results.

Table 3. VT Raman peak fitting parameters.

Parameters		MZO350	MZO450	MZO550
$A_1(\text{LO})$	Γ_0	50.1	63.3	50.4
	N_1	4.41	3.64	2.62
	N_2	1.53	1.07	0.63
	N_1/N_2	2.88	3.40	4.16
$E_1(\text{LO})$	Γ_0	35.9	26.8	29.7
	N_1	2.21	2.08	1.87
	N_2	1.21	1.02	0.85
	N_1/N_2	1.83	2.04	2.20

Tables 2 and 3 show that with the substrate-growth temperature T_s increasing from 350 °C to 550 °C, M_1/M_2 and N_1/N_2 ratios are decreased, indicating the decrease in the four-phonon process. Figure 9 further presents the variations in these two ratios versus substrate-growth temperature.

Based upon the above fittings in Table 3 on FWHM and the obtained Γ_0 , for $A_1(\text{LO})$ and $E_1(\text{LO})$ of the three $\text{Mg}_{0.1}\text{Zn}_{0.9}\text{O}$ samples, we calculated the phonon lifetimes. The phonon lifetime τ of a phonon mode obeys the energy–time uncertainty relation [48,49],

$$\Delta E = \hbar/\tau = 2\pi c\Gamma, \quad (8)$$

where ΔE is the phonon line width, and $\hbar = 5.3 \times 10^{(-12)} \text{ cm}^{-1}\cdot\text{s}$. $\tau = \hbar/\Delta E = 5.3/\Gamma_0$ (ps) can be calculated, and the obtained values are listed in Table 4. It can be seen that the phonon lifetimes of the $A_1(\text{LO})$ mode (in 0.08–0.11 ps) are shorter than those of the $E_1(\text{LO})$ mode (in 0.15–0.2 ps) for all three $\text{Mg}_{0.1}\text{Zn}_{0.9}\text{O}$ samples. Among $A_1(\text{LO})$ phonons, MZO450 has

a phonon lifetime shorter than MZO350 and MZO550, while for $E_1(\text{LO})$ with the reverse trend, MZO450 possesses a phonon lifetime longer than the other two.

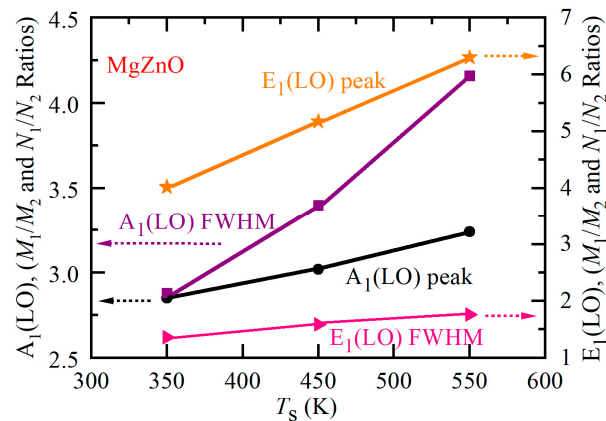


Figure 9. M_1/M_2 and N_1/N_2 versus T_s of the $\text{Mg}_{0.1}\text{Zn}_{0.9}\text{O}$ samples.

Table 4. The phonon lifetime of $A_1(\text{LO})$ and $E_1(\text{LO})$ Raman modes of samples.

Parameters		MZO350	MZO450	MZO550
$A_1(\text{LO})$	Γ_0 (cm^{-1})	50.1	63.3	50.4
	τ (ps)	0.106	0.084	0.105
$E_1(\text{LO})$	Γ_0 (cm^{-1})	35.9	26.8	29.7
	τ (ps)	0.148	0.198	0.178

In the literature search, we did not find the phonon lifetimes of ternary MgZnO alloys, so we attempted to make comparisons with those from binary ZnO and AlN semiconductors. R. Cuscó et al. [48] studied the T -dependence of Raman scattering in ZnO and obtained the phonon lifetimes at 300 K of $A_1(\text{LO})$ and $E_1(\text{LO})$ modes, which were 0.54 ps and 0.45 ps, respectively, longer than values of our MgZnO samples. B. P. Swain measured C-doped ZnO with longer phonon lifetimes [49]. The phonon lifetimes of $A_1(\text{LO})$ and $E_1(\text{LO})$ modes (in about 0.1–0.2 ps) from our $\text{Mg}_{0.1}\text{Zn}_{0.9}\text{O}$ samples were shorter than those of binary ZnO from above [48] in the literature and AlN thin films (0.4–0.8 ps) studied by us previously [50], but still at the same 0.1 ps order level. In the future, we will try to further study the phonon lifetime of $\text{Mg}_x\text{Zn}_{1-x}\text{O}$ alloys with a wide range of $x(\text{Mg})$. C. Aku-Leh et al. [51] and M. Mil-lot et al. [52] performed T -dependent Raman studies on ZnO materials and obtained the T -dependences of ZnO phonon lifetimes, which offer good references. In addition, for cases of other types of oxides, such as rutile tin dioxide (SnO_2), T. Lan et al. [53] performed variable-temperature (VT, 83–873 K) Raman studies and first-principles calculations, to assess the kinematics of three- and four-phonon processes, which generate Raman peak widths and shifts. L.K. Gaur et al. [54] investigated the phonon anharmonicity and microstructural changes of laser-power-dependent Raman spectra in Co-doped SnO_2 nanoparticles, revealed a large Raman mode broadening and shift towards the lower wavenumber side, and presented an explanation based on the kinematics of three-phonon processes.

3.4. Extended X-Ray Fine Structure (EXAFS) Investigation

Extended X-ray fine structure (EXAFS) spectroscopy is a powerful technique to investigate the crystal electronic structure, and we employed it to study the configuration of Mg and Zn atoms. We had previously performed EXAFS studies for a set of $\text{Mg}_x\text{Zn}_{1-x}\text{O}$ ($0 < x < 0.15$) layers deposited on sapphire by MOCVD [29,30]. EXAFS spectra of the Zn K -edge from our four $\text{Mg}_{0.1}\text{Zn}_{0.9}\text{O}$ samples were captured using the same technique. Subsequently, normalized and background-subtracted Zn K -edge fine structure spectra

$K^2 \cdot \chi(K)$ were obtained for our samples. Utilizing the EXAFS fitting program IFEFFIT, the Fourier-transformed fitting results of the real-space spectra were produced, as shown in Figure 10, accompanying the fitting parameters listed in Table 5.

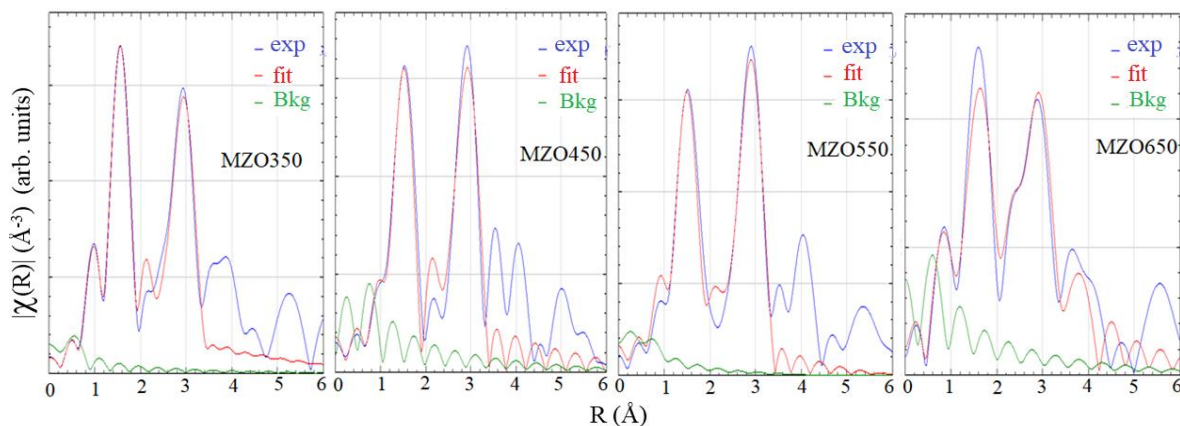


Figure 10. The Zn K-edge EXAFS and the fitting spectra of the four $\text{Mg}_{0.1}\text{Zn}_{0.9}\text{O}$ samples.

Table 5. Fitted result from the Zn K-edge EXAFS spectra for the four $\text{Mg}_{0.1}\text{Zn}_{0.9}\text{O}$ samples.

Sample No.	$R_{\text{in}}(\text{Zn-O})$ (Å)	$R_{\text{out}}(\text{Zn-O})$ (Å)	$R_{\text{in}}(\text{Zn-Zn})$ (Å)	$R_{\text{out}}(\text{Zn-Zn})$ (Å)
MZO350	1.9472	1.7649	3.1521	3.3027
MZO450	1.9394	1.7557	3.1544	3.2968
MZO550	1.9632	1.8052	3.2776	3.1530
MZO650	1.9870	1.7621	3.3171	3.1395

In Table 5, $R_{\text{in}}(\text{Zn-O})$ represents the bonding length between the nearest Zn and O atoms in the c-plane, and $R_{\text{out}}(\text{Zn-O})$ represents the bonding length between the nearest Zn and O atoms along the c-axis direction. The four nearest Zn atoms form a tetrahedral structure. $R_{\text{in}}(\text{Zn-Zn})$ represents the bonding length between the nearest Zn and Zn atoms along the a-axis direction. $R_{\text{out}}(\text{Zn-Zn})$ represents the bonding length between the nearest Zn and Zn atoms out of the c-plane. Because $x(\text{Mg})$ values are near 0.1, the two peaks in the EXAF spectra are caused mainly by Zn-O and Zn-Zn bonding. From Table 5, the nearest bonding length $R_{\text{in}}(\text{Zn-O})$ is between 1.939 and 1.987 Å, while the $R_{\text{in}}(\text{Zn-O})$ of MZO350 and MZO650 is longer than that of MZO450 and MZO550. Also, as the substrate-growth temperature T_s increases, the in-plane Zn-Zn bonding length $R_{\text{in}}(\text{Zn-Zn})$ increases, accompanying the out-of-plane Zn-Zn bonding length $R_{\text{in}}(\text{Zn-Zn})$ decreasing. This trend matches well with XRD data analysis and can be explained as follows. With the substrate-growth temperature T_s rising, Mg integrates into the hexagonal ZnO structure, leading to the increase of the surface $x(\text{Mg})$ amount and the alteration of the Zn-Zn bonding length.

4. Conclusions

$\text{Mg}_x\text{Zn}_{1-x}\text{O}$ ($x \sim 0.1$) thin films were grown on sapphire with different substrate growth temperature T_s of 350 °C, 450 °C, 550 °C, and 650 °C, respectively, by MOCVD and investigated via multiple techniques. The effects of the substrate-growth temperature T_s on the optical, structural, and surface properties of $\text{Mg}_{0.1}\text{Zn}_{0.9}\text{O}$ thin films were studied penetratively. HR-XRD data confirmed the $\text{Mg}_{0.1}\text{Zn}_{0.9}\text{O}$ (0002) diffraction, indicated that MgO phase separation occurred at a low T_s , and revealed that too-low and too-high T_s lead to the expansion of the c-axis lattice constant of the $\text{Mg}_{0.1}\text{Zn}_{0.9}\text{O}$ film. Calculations indicated that the sample with $T_s = 550$ °C had the largest crystallite size and the lowest lattice strain and dislocation density. SE measurements and analyses determined the $\text{Mg}_{0.1}\text{Zn}_{0.9}\text{O}$ film thicknesses, allowed us to chart $(\alpha \cdot h\nu)^2$ versus $h\nu$ plots, and determined their bandgap

E_g in the 3.29–3.91 eV range. The obtained α versus $h\nu$ and $\ln(\alpha)$ versus $h\nu$ relationships determined the Urbach energy E_U , between 93 and 466 meV.

UV-excitation Raman spectra exhibited the $\text{Mg}_{0.1}\text{Zn}_{0.9}\text{O}$ asymmetric 1-LO modes deconvoluted into the $A_1(\text{LO})$ and $E_1(\text{LO})$ modes. Variable-temperature (VT) Raman analyses revealed that their splitting, $\Delta\omega = \omega[A_1(\text{LO})] - \omega[E_1(\text{LO})]$, decreased with T from 80 K to 530 K. A theoretical model with three- and four-phonon processes was used to fit the T -dependent Raman shift and width. The matching trend implies that the Raman shift versus T dependences occurs mainly due to lattice expansion from the thermal dynamics process and the anharmonic process involving three- and four-phonon coupling. The $A_1(\text{LO})$ mode has a phonon lifetime τ longer than that of the $E_1(\text{LO})$ mode. MZO450 has a $\tau[A_1(\text{LO})]$ longer than those of MZO350 and MZO550, while its $\tau[E_1(\text{LO})]$ is shorter than the other two.

The Zn K -edge extended X-ray fine structure (EXAFS) investigation deduced both in-plane Zn-O and out-of-plane Zn-Zn atomic bonding lengths. The nearest bonding length $R_{\text{in}}(\text{Zn-O})$ is between 1.939 and 1.987 Å, while the $R_{\text{in}}(\text{Zn-O})$ of MZO350 and MZO650 are longer than those of MZO450 and MZO550. As the T_s increases, the in-plane Zn-Zn bonding length $R_{\text{in}}(\text{Zn-Zn})$ increases, while the out-of-plane Zn-Zn bonding length $R_{\text{out}}(\text{Zn-Zn})$ decreases. This trend matched the XRD results. As the T_s rises, more Mg integrates into the hexagonal ZnO structure, and the addition of surface Mg content results in the alteration of the Zn-Zn (Mg) bonding length.

Our results revealed that $T_s = 550$ °C is the optimal T_s for MOCVD growth of $\text{Mg}_{0.1}\text{Zn}_{0.9}\text{O}$ on sapphire substrate, and they provide valuable references for $\text{Mg}_{0.1}\text{Zn}_{0.9}\text{O}$ and other advanced materials.

Author Contributions: Conceptualization, J.L., Z.C.F., D.X. and S.L.; methodology, J.L., Z.C.F., D.X., M.T.N. and S.L.; software, J.L., D.X., M.T.N., L.W., Z.-R.Q., D.-S.W., C.Z. and J.Y.; validation, J.L., Z.C.F., D.X., H.-H.L., W.L., B.K., I.T.F. and S.L.; formal analysis, J.L., Z.C.F., D.X., M.T.N., L.W., J.Y., B.K., I.T.F. and S.L.; investigation, J.L., Z.C.F., D.X., M.T.N., L.W., D.-S.W., C.Z., J.Y. and S.L.; resources, J.L., Z.C.F., D.X., C.Z. and S.L.; data curation, J.L., Z.C.F., D.X. and S.L.; writing—original draft preparation, J.L., Z.C.F., D.X. and S.L.; writing—review and editing, J.L., Z.C.F., D.X., M.T.N., L.W., Z.-R.Q., D.-S.W., C.Z., J.Y., H.-H.L., B.K., I.T.F. and S.L.; visualization, J.L., Z.C.F., D.X., M.T.N. and S.L.; supervision, S.L.; project administration, Z.C.F. and S.L.; funding acquisition, J.L. and S.L. All authors have read and agreed to the published version of the manuscript.

Funding: This research was funded by the National Natural Science Foundation of China (Grant Nos. 52130504, 52305577, and 52205592), the Interdisciplinary Research Program of Huazhong University of Science and Technology (Grant No. 2023JCYJ047), the Innovation Project of Optics Valley Laboratory (Grant No. OVL2023PY003), the Postdoctoral Fellowship Program (Grade B) of the China Postdoctoral Science Foundation (Grant No. GZB20230244), and the Fellowship from the China Postdoctoral Science Foundation (Grant No. 2024M750995). The authors are thankful for the technical support from the Experiment Centre for Advanced Manufacturing and Technology in the School of Mechanical Science & Engineering of HUST.

Data Availability Statement: The data presented in this study are available on request from the corresponding author.

Acknowledgments: The authors are thankful for the technical support from the Experiment Centre for Advanced Manufacturing and Technology in the School of Mechanical Science & Engineering of HUST.

Conflicts of Interest: Weijie Lu is employed by Hexagonal Scientific Laboratory, LLC. The remaining authors declare that the research was conducted in the absence of any commercial or financial relationships that could be construed as a potential conflict of interest.

References

1. Borysiewicz, M.A. ZnO as a Functional Material, a Review. *Crystals* **2019**, *9*, 505. [[CrossRef](#)]
2. Kumar, P.; Malik, H.K.; Gautam, S.; Chae, K.H.; Asokan, K.; Kanjilal, D. Modifications in Room Temperature Ferromagnetism by Dense Electronic Excitations in $\text{Zn}_{0.9}\text{Mg}_{0.1}\text{O}$ Thin Films. *J. Alloys Compd.* **2017**, *710*, 831–835. [[CrossRef](#)]

3. Chen, H.; Yu, P.; Zhang, Z.; Teng, F.; Zheng, L.; Hu, K.; Fang, X. Ultrasensitive Self-Powered Solar-Blind Deep-Ultraviolet Photodetector Based on All-Solid-State Polyaniline/MgZnO Bilayer. *Small* **2016**, *12*, 5809–5816. [[CrossRef](#)] [[PubMed](#)]
4. Kara, R.; Mentar, L.; Azizi, A. Synthesis and Characterization of Mg-doped ZnO Thin-Films Electrochemically Grown on FTO Substrates for Optoelectronic Applications. *RSC Adv.* **2020**, *10*, 40467–40479. [[CrossRef](#)]
5. Pandey, R.; Shimpi, T.; Munshi, A.; Sites, J.R. Impact of Carrier Concentration and Carrier Lifetime on MgZnO/CdSeTe/CdTe Solar Cells. *IEEE J. Photovolt.* **2020**, *10*, 1918–1925. [[CrossRef](#)]
6. Tsai, D.-C.; Chen, F.-K.; Chang, Z.-C.; Kuo, B.-H.; Chen, E.-C.; Huang, Y.-L.; Shieu, F.-S. Effect of Al₂O₃-Doping on the Structure and Optoelectronic Characteristics of MgZnO Thin Film Prepared by RF Magnetron Sputtering. *Appl. Phys. A* **2021**, *127*, 571. [[CrossRef](#)]
7. Razooqi Alaani, M.A.; Koirala, P.; Phillips, A.B.; Liyanage, G.K.; Awni, R.A.; Sapkota, D.R.; Balaji, R.; Heben, M.J.; O’Leary, S.K.; Podraza, N.J.; et al. Optical Properties of Magnesium-Zinc Oxide for Thin Film Photovoltaics. *Materials* **2021**, *14*, 5649. [[CrossRef](#)]
8. Jamarkattel, M.K.; Phillips, A.B.; Li, D.B.; Bastola, E.; Liyanage, G.K.; Friedl, J.D.; Bista, S.S.; Pokhrel, D.; Quader, A.; Kaluarachchi, P.N.; et al. High Vacuum Heat Treated MZO: Increased n-type Conductivity and Elimination of S-kink in MZO/CdSe/CdTe Solar Cells. *MRS Adv.* **2022**, *7*, 713–717. [[CrossRef](#)]
9. Li, Y.; Yu, F.; Li, G.; Lu, M.; Lu, Y. MgZnO High-Voltage Transparent Thin-Film Transistors Built on Glass. *Phys. Status Solidi A* **2022**, *219*, 2200313. [[CrossRef](#)]
10. Zhang, B.; Liu, R.; Kimura, H.; Dou, Y.; Dai, Z.; Xiao, L.; Ni, C.; Hou, C.; Sun, X.; Yu, R.; et al. Phase Transformation and Performance of Mg-Based Hydrogen Storage Material by Adding ZnO Nanoparticles. *Nanomaterials* **2023**, *13*, 1321. [[CrossRef](#)]
11. Liu, J.; Zhou, Z.; Gu, H.; Zhu, J.; Jiang, H.; Liu, S. Asymmetric optical properties and bandgap shift of pre-strained flexible ZnO films. *APL Mater.* **2024**, *12*, 041126. [[CrossRef](#)]
12. Chen, Z.; Wang, J.; Wu, H.; Yang, J.; Wang, Y.; Zhang, J.; Bao, Q.; Wang, M.; Ma, Z.; Tress, W.; et al. A transparent electrode based on solution-processed ZnO for organic optoelectronic devices. *Nat. Commun.* **2022**, *13*, 4387. [[CrossRef](#)] [[PubMed](#)]
13. Choopun, S.; Vispute, R.D.; Yang, W.; Sharma, R.P.; Venkatesan, T. Realization of band gap above 5.0 eV in metastable cubic-phase Mg_xZn_{1-x}O alloy films. *Appl. Phys. Lett.* **2002**, *80*, 1529. [[CrossRef](#)]
14. Seghir, B.B.; Hima, M.; Moulatti, F.; Sahraoui, I.; Ben Amor, L.; Zeghoud, S.; Hemmami, H.; Kouadri, I.; Ben Amor, A.; Messaoudi, M.; et al. Exploring the Antibacterial Potential of Green-Synthesized MgO and ZnO Nanoparticles from Two Plant Root Extracts. *Nanomaterials* **2023**, *13*, 2425. [[CrossRef](#)]
15. Przedziecka, E.; Paradowska, K.M.; Jakiela, R.; Kryvyi, S.; Zielony, E.; Placzek-Popko, E.; Lisowski, W.; Sybilski, P.; Jarosz, D.; Adhikari, A.; et al. Polar and Non-Polar Zn_{1-x}Mg_xO: Sb Grown by MBE. *Materials* **2022**, *15*, 8409. [[CrossRef](#)] [[PubMed](#)]
16. Gnanasambandan, P.; Adjeroud, N.; Leturcq, R. Role of ZnO and MgO Interfaces on the Growth and Optoelectronic Properties of Atomic Layer Deposited Zn_{1-x}Mg_xO films. *J. Vac. Sci. Technol. A* **2022**, *40*, 062413. [[CrossRef](#)]
17. Falson, J.; Kawasaki, M. A review of the quantum Hall effects in MgZnO/ZnO heterostructures. *Rep. Prog. Phys.* **2018**, *81*, 056501. [[CrossRef](#)]
18. Mishra, M.; Saha, R.; Tyagi, L.; Sushama, S.; Pandey, S.K.; Chakrabarti, S. Investigation of Phosphorus-Doping of MgZnO Thin Films Using Efficient Spin-on Dopant Process. *J. Lumin.* **2023**, *257*, 119748. [[CrossRef](#)]
19. Han, T.; Kutlu-Narin, E.; Narin, P.; Sarikavak-Lisesivdin, B.; Lisesivdin, S.B. Structural and Optical Properties of Mist-CVD grown MgZnO: Effect of Precursor Solution Composition. *Phys. B* **2023**, *659*, 414854. [[CrossRef](#)]
20. Hoang, M.-S.; Chen, H.-S. Cubic- and Hexagonal-Phase MgZnO Nanoparticles for Electron Transport Layers in Electroluminescent Quantum-Dot Light-Emitting Diodes. *ACS Appl. Nano Mater.* **2023**, *6*, 15294–15301. [[CrossRef](#)]
21. Tsay, C.-Y.; Chen, S.-T.; Tsai, H.-M. Tailoring of the Structural, Optical, and Electrical Characteristics of Sol-Gel-Derived Magnesium-Zinc-Oxide Wide-Bandgap Semiconductor Thin Films via Gallium Doping. *Materials* **2023**, *16*, 6389. [[CrossRef](#)] [[PubMed](#)]
22. Ganesha, K.V.S.; Mahesha, M.G. (Mg, Mn)-Dual Doping Synergism Towards Luminescence and Electrical Properties of ZnO/p-Si Heterojunction Diodes. *RSC Adv.* **2023**, *13*, 32282. [[CrossRef](#)]
23. Chen, S.; Wang, N.; Wang, Y.; Xie, Q.; Pan, X.; He, H.; Wang, F.; Suo, H.; Ye, Z. Compliant Substrate Epitaxial MgZnO Films Using Fluorophlogopite Mica Approaching Homoepitaxy Quality. *Appl. Surf. Sci.* **2024**, *653*, 159439. [[CrossRef](#)]
24. Heng, C.L.; Li, X.L.; Wang, X.; Su, W.Y.; Finstad, T.G. Effects of Ytterbium Doping on the Ultraviolet Emissions of MgZnO Films Prepared by Magnetron Sputtering. *J. Alloys Compd.* **2024**, *981*, 173704. [[CrossRef](#)]
25. Tokai, S.; Yanagitani, T. Full-Epitaxial ScAlN and MgZnO Solidly Mounted Resonators Based on Epitaxial Acoustic Bragg Reflector. *Appl. Phys. Lett.* **2024**, *124*, 082901. [[CrossRef](#)]
26. Šermukšnis, E.; Šimukovic, A.; Avrutin, V.; Izyumskaya, N.; Ozgur, U.; Morkoc, H. Hot-Electron Microwave Noise and Energy Relaxation in (Be)MgZnO/ZnO Heterostructures. *Crystals* **2024**, *14*, 75. [[CrossRef](#)]
27. Wu, C.C.; Wu, D.S.; Lin, P.R.; Chen, T.N.; Horng, R.H.; Ou, S.L.; Tu, Y.L.; Wei, C.C.; Feng, Z.C. Characterization of Mg_xZn_{1-x}O Thin Films Grown on Sapphire Substrates by Metalorganic Chemical Vapor Deposition. *Thin Solid Films* **2011**, *519*, 1966–1970. [[CrossRef](#)]
28. Azeem, W.; Su, S.; Ho, L.P.; Younas, M.; Azad, F.; Rashid, R. Point contact bipolar resistive switching observed in transparent ZnMgO/ZnO:Ga heterostructure. *J. Mater. Sci.-Mater. El.* **2019**, *30*, 700. [[CrossRef](#)]
29. Chetia, S.K.; Rajput, P.; Ajimsha, R.S.; Singh, R.; Das, A.K.; Kumar, R.; Padhi, P.S.; Sinha, A.K.; Jha, S.N.; Sharma, T.K.; et al. Bandgap tunability and local structure of Mg_xZn_{1-x}O (0 ≤ x ≤ 1) thin films grown by RF magnetron co-sputtering. *Appl. Phys. A* **2022**, *128*, 724. [[CrossRef](#)]
30. Zheng, W.; Lin, H.-H.; Feng, Z.C.; Chang, F.-H.; Lee, J.-F.; Liu, C.W.; Wu, D.-S.; Zheng, R.S. Lattice Deformation of Wurtzite Mg_xZn_{1-x}O Alloys: An Extended X-ray Absorption Fine Structure Study. *J. Alloys Compd.* **2014**, *582*, 157–160. [[CrossRef](#)]

31. Bergman, L.; Morrison, J.L.; Chen, X.-B.; Huso, J.; Hoeck, H. Ultraviolet Photoluminescence and Raman Properties of MgZnO Nanopowders. *Appl. Phys. Lett.* **2006**, *88*, 023103. [[CrossRef](#)]
32. Wang, L.; Ma, J.; Xu, H.; Zhang, C.; Li, X.; Liu, Y. Anisotropic strained cubic MgZnO/MgO multiple-quantum-well nanorods: Growths and optical properties. *Appl. Phys. Lett.* **2013**, *102*, 031905. [[CrossRef](#)]
33. Sfuncia, G.; Nicotra, G.; Giannazzo, F.; Péc, B.; Gueorguiev, G.K.; Kakanakova-Georgieva, A. 2D graphitic-like gallium nitride and other structural selectivity in confinement at the graphene/SiC interface. *CrystEngComm* **2023**, *25*, 5810–5817. [[CrossRef](#)]
34. Filho, M.A.M.; Farmer, W.; Hsiao, C.-L.; dos Santos, R.B.; Hultman, L.; Birch, J.; Ankit, K.; Gueorguiev, G.K. Density functional theory-fed phase field model for semiconductor nanostructures: The case of self-induced core-shell InAlN nanorods. *Cryst. Growth Des.* **2024**, *24*, 4717–4727. [[CrossRef](#)] [[PubMed](#)]
35. Sanam, M.; Shah, Z.H.; Ullah, F.; Khalil, M.; Ramay, S.M.; Saleem, M. Structural, electronic, and optical study of Zn: MgO compositions by computational and experimental approach. *Ceram. Int.* **2024**, *50*, 28078–28086. [[CrossRef](#)]
36. Schreyer, M.; Guo, L.; Thirunahari, S.; Gao, F.; Garland, M. Simultaneous Determination of Several Crystal Structures from Powder Mixtures: The Combination of Powder X-ray Diffraction, Band-Target Entropy Minimization and Rietveld Methods. *J. Appl. Crystallogr.* **2014**, *47*, 659–667. [[CrossRef](#)]
37. Palik, E.D. *Handbook of Optical Constants of Solids*; Elsevier: London, UK, 1997.
38. Liu, Y.; Yang, Z.; Long, X.; Zhang, X.; Wei, J.; Huang, D.; Ferguson, I.T.; Feng, Z.C. Effects of Thickness and Interlayer on Optical Properties of AlN Films at Room and High Temperature. *J. Vac. Sci. Technol. A* **2021**, *39*, 043402. [[CrossRef](#)]
39. Yang, Y.; Liu, Y.; Wang, L.; Zhang, S.; Lu, H.; Peng, Y.; Wei, W.; Yang, J.; Feng, Z.C.; Wan, L.; et al. Optical and Structural Properties of Aluminum Nitride Epi-Films at Room and High Temperature. *Materials* **2023**, *16*, 7442. [[CrossRef](#)]
40. Rambadey, O.V.; Kumar, A.; Sati, A.; Sagdeo, P.R. Exploring the Interrelation between Urbach Energy and Dielectric Constant in Hf-Substituted BaTiO₃. *ACS Omega* **2021**, *6*, 32231–32238. [[CrossRef](#)]
41. Huso, J.; Morrison, J.L.; Hoeck, H.; Casey, E.; Bergman, L.; Pounds, T.D.; Norton, M.G. Low Temperature LO-Phonon Dynamics of MgZnO Nanoalloys. *Appl. Phys. Lett.* **2007**, *91*, 111906. [[CrossRef](#)]
42. Jiang, T.; Xu, S.; Zhang, J.; Li, P.; Huang, J.; Niu, M.; Meng, X.; Chen, Z.; Zhu, J.; Zhao, Y.; et al. Temperature dependence of the Raman-active modes in the semipolar (11 $\bar{2}$) plane GaN Film. *J. Appl. Phys.* **2016**, *120*, 245706. [[CrossRef](#)]
43. Kumar Yadav, H.; Katiyar, R.S.; Gupta, V. Temperature dependent dynamics of ZnO nanoparticles probed by Raman scattering: A big divergence in the functional areas of nanoparticles and bulk materials. *Appl. Phys. Lett.* **2012**, *100*, 051906. [[CrossRef](#)]
44. Ferguson, I.T.; Qiu, Z.R.; Wan, L.; Yiin, J.; Klein, B.; Feng, Z.C. Multiple Raman Scattering Spectroscopic Studies of Crystalline Hexagonal SiC Crystals, Chapter 9. In *Handbook of Silicon Carbide Materials and Devices*; Zhe, C.F., Ed.; CRC/Taylor & Francis: London, UK, 2023; pp. 219–248.
45. Bundesmann, C.; Rahm, A.; Lorenz, M.; Grundmann, M.; Schubert, M. Infrared Optical Properties of Mg_xZn_{1-x}O Thin Films (0 < x < 1) Long-Wavelength Optical Phonons and Dielectric Constants. *J. Appl. Phys.* **2006**, *99*, 113504. [[CrossRef](#)]
46. Choi, H.J.; Jung, Y.S.; Han, J.; Cho, Y.S. In-situ stretching strain-driven high-piezoelectricity and enhanced electromechanical energy-harvesting performance of a ZnO nanorod-array structure. *Nano Energy* **2020**, *72*, 104735. [[CrossRef](#)]
47. Huso, J.; Che, H.; Thapa, D.; Canul, A.; McCluskey, M.D.; Bergman, L. Phonon Dynamics and Urbach Energy Studies of MgZnO Alloys. *J. Appl. Phys.* **2015**, *117*, 125702. [[CrossRef](#)]
48. Cuscó, R.; Alarcón-Lladó, E.; Ibáñez, J.; Artús, L.; Jiménez, J.; Wang, B.; Callahan, M.J. Temperature Dependence of Raman Scattering in ZnO. *Phys. Rev. B* **2007**, *75*, 165202. [[CrossRef](#)]
49. Swain, B.P. Investigation of Fractal Behavior, Optical Properties and Electronic Environments of Carbon Doped of ZnO Thin Films. *Appl. Phys. A* **2021**, *127*, 375. [[CrossRef](#)]
50. Feng, Z.C.; Yang, H.; Wan, L.; Wu, F.; Dia, J.; Chen, C.; Saravade, V.; Yiin, J.; Klein, B.; Ferguson, I.T. Crystalline and Optical Properties of AlN Films with Varying Thicknesses (0.4–10 μm) Grown on Sapphire by Metalorganic Chemical Vapor Preposition. *Thin Solid Films* **2023**, *780*, 139939. [[CrossRef](#)]
51. Aku-Leh, C.; Zhao, J.; Merlin, R.; Menéndez, J.; Cardona, M. Long-lived Optical Phonons in ZnO Studied with Impulsive Stimulated Raman Scattering. *Phys. Rev. B* **2005**, *71*, 205211. [[CrossRef](#)]
52. Millot, M.; Tena-Zaera, R.; Munoz-Sanjose, V.; Broto, J.-M.; Gonzalez, J. Anharmonic Effects in ZnO Optical Phonons Probed by Raman Spectroscopy. *Appl. Phys. Lett.* **2010**, *96*, 152103. [[CrossRef](#)]
53. Lan, T.; Li, C.W.; Fultz, B. Phonon anharmonicity of rutile SnO₂ studied by Raman spectrometry and first principles calculations of the kinematics of phonon-phonon interactions. *Phys. Rev. B* **2012**, *86*, 134302. [[CrossRef](#)]
54. Gaur, L.K.; Mathpal, M.C.; Kumar, P.; Gairola, S.P.; Agrahari, V.; Martinez, M.A.R.; Aragon, F.F.H.; Soler, M.A.G.; Swart, H.C.; Agarwal, A. Observations of phonon anharmonicity and microstructure changes by the laser power dependent Raman spectra in Co doped SnO₂ nanoparticles. *J. Alloys Compd.* **2020**, *831*, 154836. [[CrossRef](#)]

Disclaimer/Publisher's Note: The statements, opinions and data contained in all publications are solely those of the individual author(s) and contributor(s) and not of MDPI and/or the editor(s). MDPI and/or the editor(s) disclaim responsibility for any injury to people or property resulting from any ideas, methods, instructions or products referred to in the content.